J. Fluid Mech. (1981), *vol.* 107, *pp.* 375–406
Printed in Great Britain

Numerical study of small-scale intermittency in three-dimensional turbulence

By ERIC D. SIGGIA

Laboratory of Atomic and Solid State Physics, Cornell University, Ithaca, New York 14853, and National Center for Atmospheric Research, P.O. Box 3000, Boulder, Colorado 80307

(Received 2 October 1979 and in revised form 27 August 1980)

Intermittency effects, in magnitude comparable to the early Batchelor & Townsend (1949) experiments, are studied for stationary, homogeneous, isotropic turbulence by means of a direct spectral simulation on a 64^3 lattice. The turbulence is kept stationary by a coupling to modes external to the spectral code that model the straining effects of large scales on smaller ones. The rate of energy input and viscosity are free parameters. The interrelations of intermittency and parametrizations of the large scales are discussed. Small-scale universality and a local cascade are necessary if comprehensive models of the large scales are to prove tractable. An iterative method to determine the otherwise arbitrary parameters in such a scheme is proposed but not implemented.

The equations for energy and vorticity balance are checked as a function of wavenumber. The nonlinear (e.g. vortex stretching) terms in the spectral simulation account for nearly 95 % of the vorticity production with the external forcing supplying the rest. The non-dimensionalized one-dimensional energy spectrum agrees well with experiments in the dissipation range at $R_\lambda \sim 100$. The locality of the energy cascade in wavenumber is also examined.

First- and second-derivative flatness factors of order 4·5–5·0 and 9·0 respectively are found under stationary conditions with bursts to higher values. Resolution and other systematic errors are explored by extensive runs with a 32^3 code; de-aliasing all higher-order derivative statistics; and recomputing selected averages after zeroing in succession the highest- and lowest-wavenumber bands. The latter analysis is of some relevance to the experimental problem of gauging how a finite-length hot wire biases a flatness measurement. A host of other higher-order derivative statistics are computed, including the vorticity/rate of strain correlations. Three-dimensional plots of the vorticity reveal persistent and extended tubes, sheets and blobs.

1. Introduction

It has long been obvious that the direct numerical simulation of three-dimensional turbulent flows will never reach the Reynolds numbers that are routinely attainable in the laboratory. Nevertheless, much useful information about the large scales of motion has been obtained numerically by parametrizing how scales too small to be resolved act back on those being simulated. Since our interests here are the small scales of motion and intermittency, we were led to consider the converse problem of modelling the large scales of motion. In the following paragraphs, we will outline, in analogy with subgrid modelling, how to assess the validity of models of the large

scales and fix the parameters that enter them. We will then discuss why the existence of small-scale intermittency greatly complicates such a modelling effort. Our discussion will be phrased in terms of homogeneous isotropic flows.

Imagine a computer code designed to simulate the Navier–Stokes equations over a range of wavenumbers, k, satisfying $k_0 \leqslant k < \Lambda$. To test a subgrid model, one would first simulate all wavenumbers up to Λ using ordinary viscous dissipation. A second code, restricted to $k_0 \leqslant k < \frac{1}{2}\Lambda$, together with some subgrid model would then be run forward from the same initial conditions. The free parameters in the model are to be adjusted to obtain the best fit between the large-scale statistics of the two runs. These parameters could then be used in conjunction with the larger simulation and a second iteration done. This methodology is predicated on the belief that the statistics of the large scales are Reynolds-number independent for large R_λ. In particular, with a sufficiently large code, any subgrid model that provided enough dissipation at high k should suffice. The considerable effort that has gone into subgrid modelling is directed toward finding the model that gives the most accurate large-scale statistics for fixed Λ/k_0 (Clark, Ferziger & Reynolds 1979). The methods' convergence, as Λ_0/k_0 and R_λ tend to infinity, is not at issue.

A model of the large scales is in essence a technique of forcing the remaining scales that are actually in the computer. The determination of the optimal scheme (formally defined by a set of parameters P_0), proceeds in analogy to the above paragraph up to a point. Run a simulation spanning $k_0 \leqslant k < \Lambda$ and determine a comprehensive set of small-scale statistics. They will of course depend on the viscosity or whatever other dissipation *Ansatz* was used. Now run a second simulation covering $2k_0 \leqslant k < \Lambda$, with the same dissipation as before, and adjust the new forcing parameters, P_1, so as to reproduce the small-scale statistics of the larger simulation. The ratio Λ/k_0 should be sufficiently large so that the determination of P_1 from P_0 is unaffected by the arbitrary choice of dissipation.

Among the parameters P_1 must surely be included the rate of energy input, ϵ, since it determines the principal features of the energy spectrum. Let us define a relevant parameter to be one whose adjustment is required if the small-scale statistics are to ultimately match for Λ/k_0 arbitrarily large. If Kolmogorov's 1941 theory were strictly true, ϵ would be the only relevant parameter. Having correctly set ϵ, one could examine the other elements of P_1 with a view toward accelerating the convergence between the two simulations for finite Λ/k_0. However, Kolmogorov's 1941 theory is not correct since the small scales are not Reynolds-number independent. Small-scale intermittency destroys the simple analogy that would otherwise exist between subgrid and supergrid modelling.

Intermittency, it is generally believed, grows with the range of accessible scales, other parameters being constant (Monin & Yaglom 1975). A simulation covering $k_0 \leqslant k < \Lambda$ will, for instance, give a larger velocity derivative flatness than one covering $2k_0 \leqslant k < \Lambda$ with ϵ and the dissipation being held fixed even if Λ/k_0 is arbitrarily large. (The flatness factor of a quantity γ with mean zero is defined as $F_\gamma = \langle\gamma^4\rangle/\langle\gamma^2\rangle^2$.) In the above nomenclature, there must be other relevant variables in addition to ϵ to compensate for the missing octave of wavenumbers, $k_0 \leqslant k < 2k_0$, in the smaller simulation. To make the two simulations match statistically on the small scales, it is perhaps plausible to let ϵ fluctuate about the mean set by the larger simulation (Kraichnan 1974; Mandelbrot 1976; Frisch, Sulem & Nelkin 1978). To

accomplish this, in practice, requires a model for the time dependence of ϵ rather than just its probability distribution (Siggia 1977, 1978). Whether all relevant parameters, in the sense defined above, relate to ϵ and its fluctuations is not known. The degree of small-scale universality that exists among flows with very different large-scale features (jets, wakes, boundary layers) suggests that there are not too many relevant parameters.

Intermittency greatly complicates the numerical study of small-scale or dissipation-range statistics at high R_λ. Whereas the large scales are Reynolds-number independent for large R_λ, here one is required to consider explicitly a Reynolds-number dependence and address a more complicated question than arose with subgrid models, namely how to simulate a much wider range of scales than can be directly accommodated in one's computer. This problem is not intractable if there are sufficiently few relevant variables and an accurate forcing parametrization can be devised.

Simply stated, use the parameters P_1 obtained as above as input to a simulation spanning $2k_0 \leqslant k < 2\Lambda$. Determine small-scale statistics and match to the analogous quantities obtained from a simulation spanning $4k_0 \leqslant k < 2\Lambda$ by adjusting the new forcing parameters P_2. After each iteration, the viscosity can be decreased so as to increase R_λ by roughly $2^{\frac{1}{2}}$. The elements of P_i characterizing the intermittency should increase secularly with the iteration number i.

The program we have outlined can prove impossible to implement in a number of different ways. The cascade may be quite non-local and require a larger simulation than is now feasible to encompass it. Lack of universality (i.e. many relevant parameters) is another difficulty that could render any large-scale parametrization unmanageable. The latter problem is of physical interest and under favourable circumstances one might hope to isolate the large-scale perturbation whose influence is felt on the small scales. Somewhat unexpectedly, very long integration times were needed to obtain accurate statistics owing to the appearance of temporal intermittency, whose manifestations were a few rare but violent events that dominated small-scale statistics. Insufficient machine time has prevented us from doing much more than an initial comparison of runs covering different scale ranges and an examination of sensitivity to certain forcing parameters. Non-local interactions were not a problem; and, in following the time development, various measures of intermittency moved together, suggesting some element of universality. Apart from our iterative scheme, the simulations permit a detailed examination of many manifestations of small-scale intermittency. Although the Reynolds number is still modest, there is no doubt about the existence of intermittency.

In the following section, the numerical techniques are summarized with particular attention to the large-scale modelling. In §3(*a*), we tabulate and discuss the global (e.g. volume-averaged) parameters associated with our numerical runs. The behaviour of the forcing as well as the energy and vorticity balance together with appropriate spectra constitute §3(*b*). In §3(*c*), we collect all data relating to intermittency. This includes the flatness and related quantities for the first and second velocity derivatives, two-point vorticity correlation functions, and three-dimensional pictures of the mean-square vorticity that bring out the structures. In the conclusion, §4, we review the experimental situation in the light of our numerical results.

2. Large-scale parametrizations

Our spectral code is identical with the one used by Siggia & Patterson (1978) and Orszag & Patterson (1972) with suitable technical modifications to make it compatible with the Cray-1 computer and some minor additions to implement the forcing. The nonlinear terms were de-aliased following the Patterson & Orszag (1971) algorithm, although with a spectrum as steep as we were using this was probably unnecessary.

We have argued in § 1 why an accurate parametrization of the large scales will be considerably more delicate than the analogous problem for the small scales. Most of our numerical runs, and all the ones we discuss in detail here, were done by using modes external to the spectral code to implement the forcing. We believe our model is quite close to the correct physics since it reproduces the exact energy and vorticity balance equations as a function of wavenumber and has the additional virtue of maximizing the Reynolds number and thereby the level of intermittency that can be obtained from a given spectral code. The only way to verify definitively the completeness of our model forcing is through the iterative scheme we have outlined in § 1. Since the results of the next several sections all indicate that small-scale statistics are insensitive to the large scales, we believe that the intermittency we observe is as real as what can be measured in a small laboratory wind tunnel. Nevertheless, to guard against some unforeseen error, we have redone several runs with a completely different forcing scheme, discussed at the end of this section, that reproduces exactly the coupling implied by the Navier–Stokes equations between the forcing modes and the 'fluid' modes. Fidelity of interaction is obtained at the expense of a smaller R_λ and less intermittency. Except for differences that can be plausibly attributed to the smaller R_λ, small-scale statistics were qualitatively unchanged.

Consider an artificial partition at a wavenumber k_0 separating the velocity

$$\mathbf{v}(x) = \mathbf{v}_<(x) + \mathbf{v}_>(x)$$

into two pieces, $\mathbf{v}_<$ and $\mathbf{v}_>$, that derive respectively from wavenumbers less than and greater than k_0. The equation for the time derivative of $\mathbf{v}_>$ will have three terms that depend on $\mathbf{v}_<$. The first, symbolically $\mathbf{v}_<.\nabla\mathbf{v}_<$, is independent of $\mathbf{v}_>$ and would appear like an inhomogeneous forcing term in the equation for $\partial\mathbf{v}_>/\partial t$. It directly affects only wavenumbers $k < 2k_0$. Of the two remaining terms, $\mathbf{v}_<.\nabla\mathbf{v}_>$ does not enter the energy balance equation. That is, if we imagine integrating $\partial v_>^2/\partial t$ over a bounded or periodically continued region, the energy input from $\mathbf{v}_<.\nabla\mathbf{v}_>$ integrates to zero. The remaining term, $\mathbf{v}_>.\nabla\mathbf{v}_<$, is responsible for all the energy transfer. In fact, only the rate of strain due to $\mathbf{v}_<$ enters the equation for $\partial\int v_>^2/\partial t$.

The model we have therefore adopted to represent the coupling of all degrees of freedom with $k < k_0$ to the modes in our spectral code is:

$$\frac{\partial\mathbf{v}_k}{\partial t} = -P_k(\mathbf{S}(t).\mathbf{v}_k + i\sum_q \mathbf{v}_{k-q}.\mathbf{q}\mathbf{v}_q + \nu k^2\mathbf{v}_k), \tag{2.1}$$

where $\mathbf{S}$ is a symmetric, traceless matrix perpendicular to k and P_k is the transverse projection operator, $P_k^{ab} = (\delta^{ab} - k^a k^b/k^2)$. The forcing term in (2.1) is trivially compatible with a spectral code since $\mathbf{S}$ depends only on time.

Clearly (2.1) is a poor representation of the large-scale strain for $k_0 \leqslant k < 2k_0$, since we have not attempted to model $\mathbf{v}_<.\nabla\mathbf{v}_<$ and have neglected the r dependence

of $\nabla \mathbf{v}_<$. We will verify below that errors in the first wavenumber band have a small effect on intermittent quantities. A more serious omission is the term, $\mathbf{v}_<.\nabla \mathbf{v}_>$, which one would be tempted to model as $S^{ab}r^b\nabla^a \mathbf{v}_>$. An explicit dependence on a spatial co-ordinate is very awkward to handle with a spectral code since the Fourier transform of r is not absolutely convergent, and its derivative cannot be computed simply by multiplying by the wavenumber.

It is necessary, however, to include $\mathbf{v}_<.\nabla \mathbf{v}_>$ if the transverse part of the velocity equation is to reproduce the correct linearized equations for vortex stretching in the straining field generated by $\mathbf{v}_<$. Equation (2.1) does not satisfy this requirement even though the integrated equations for the energy and vorticity balance are correct, namely:

$$\frac{1}{2}\frac{\partial \sum_k |\mathbf{v}_k|^2}{\partial t} = -\sum_k \mathbf{v}_{-k}.\mathbf{S}.\mathbf{v}_k - \nu \sum_k k^2 |\mathbf{v}_k|^2, \tag{2.2a}$$

$$\frac{1}{2}\frac{\partial}{\partial t}\sum_k |\boldsymbol{\omega}_k|^2 = \sum_k \boldsymbol{\omega}_{-k}.\mathbf{S}.\boldsymbol{\omega}_k + \sum_k i\omega^a_{-k}(\boldsymbol{\omega}_{k-q}.\mathbf{q}v^a_q - \mathbf{v}_{k-q}.\mathbf{q}\omega^a_q) - \nu \sum_k k^2 |\boldsymbol{\omega}_k|^2. \tag{2.2b}$$

The second cubic term in (2.2*b*) of course vanishes when summed over all k but is in general non-zero when summed over a band of wavenumbers as we will do when computing spectra. The derivation of (2.2*b*) from (2.1) requires the identity

$$(\mathbf{k}\times\boldsymbol{\omega}).\mathbf{S}.(\mathbf{k}\times\boldsymbol{\omega}) = -k^2\boldsymbol{\omega}.\mathbf{S}.\boldsymbol{\omega},$$

which holds provided $\operatorname{tr}\mathbf{S} = 0$, $S^{ab} = S^{ba}$, and $\mathbf{k}.\mathbf{S} = 0$; $\operatorname{tr}\mathbf{S}$ is the trace of the matrix $\mathbf{S}$. For our actual runs, in excess of 90 % of the vorticity was produced by the nonlinear term $\omega_a\boldsymbol{\omega}.\nabla v_a$, which is of course simulated correctly, so we do not believe that the neglect of $\mathbf{v}_<.\nabla \mathbf{v}_>$ is too serious.

We have now to model the time dependence of the rate-of-strain matrix, S^{ab}, due to the large scales. Let $\mathbf{G}$ run over the set of 26 wavenumbers of the form $\frac{1}{2}k_0(n_1, n_2, n_3)$, where $n_i = 0, \pm 1$, and $G^2 > 0$. Then consider the system of equations for velocity modes $\mathbf{u}_G$ (Siggia 1977),

$$\frac{\partial u_G}{\partial t} = P_G\left(\frac{\epsilon(t)\,\mathbf{u}_G}{2E_u} - i\alpha \sum_{G'} \mathbf{u}_{G-G'}.\mathbf{G}'\mathbf{u}_{G'} - \eta\mathbf{u}_G\right), \tag{2.3}$$

where P is again the transverse projection operator,

$$E_u = \tfrac{1}{2}\sum_G |\mathbf{u}_G|^2,$$

and α is a free parameter. If we now set

$$S^{ab} = \frac{i}{2}\sum_G G^a u^b_G + G^b u^a_G, \tag{2.4}$$

and determine the eddy damping η from

$$\eta = \tfrac{1}{2}\sum_k \mathbf{v}_{-k}.\mathbf{S}.\mathbf{v}_k/E_u, \tag{2.5}$$

we find that

$$\frac{\partial}{\partial t}(E_u + E_v) = \epsilon(t) - \nu\sum_k k^2|\mathbf{v}_k|^2,$$

where $E_v = \frac{1}{2}\Sigma|\mathbf{v}_k|^2$. Energy is transferred conservatively between the u and v modes and $\epsilon(t)$ is the rate of energy input into the combined system.

The large-scale parametrization represented by (2.1), (2.3)–(2.5) has many practical virtues. The energy input, ϵ, can be specified as an independent parameter and it is

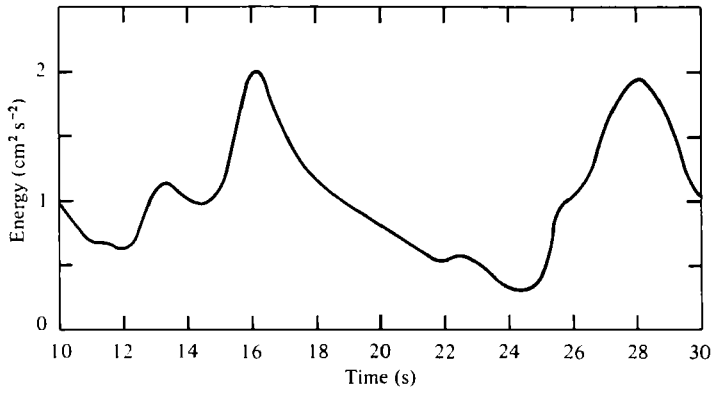

FIGURE 1. The energy in modes $2 \leqslant k < 32$ as a function of time for a portion of run 1*a* (table 1) after initial conditions have relaxed.

simple to insert non-trivial models for its time dependence. The parameter α governs the rate of phase mixing among the large scales. A zero value would model a static strain. One would like to determine, through the iterative scheme outlined in §1, the optimal value of α.

Note that we have not included a term in (2.3) that could be used to adjust the determinant of **S** although such a parameter might prove to be relevant. Betchov (1956) has shown that the determinant of the rate-of-strain matrix is related to the skewness in homogeneous isotropic turbulence. On average det (**S**) should be negative. We have monitored det (**S**) as our simulation evolves and have found no correlation between the geometry of the small-scale structures and the sign of det (**S**).

The time integration is initialized with Gaussian random velocity modes having a prescribed spectrum. A skewness is quickly established and somewhat more slowly, though in much less than a large eddy-turnover time,

$$\sum_k \mathbf{v}_{-k} . \mathbf{S} . \mathbf{v}_k$$

reaches a value of order ϵ. Equations (2.1), (2.3)–(2.5) permit an exchange of energy between the u and v modes that can deviate considerably from ϵ for short periods of time. Figure 1 shows a segment of the time record. In spite of the fluctuations, the system is stable and a time average of the dissipation in (2.1) equals ϵ (see also Siggia 1977).

If one believes, as we do, that local interactions in wavenumber suffice to explain the experimentally observed small-scale intermittency in three dimensions, the fluctuations between the u and v modes effectively boost the Reynolds number of the simulation beyond what one would compute for the spectral code in isolation. We believe that intermittency develops as the cascade proceeds and, the larger the range of scale sizes available, the greater will be the intermittency. It may be objected that the coupling represented by (2.1), (2.4) and (2.5) is not a faithful representation of the Navier–Stokes equations and that the intermittency thereby generated is not the same as what is seen experimentally. Whether this is indeed true depends on the degree of universality of the small scales or alternatively on what are the relevant variables. We will present comparative data below from 32^3 and 64^3 simulations that shared a

common upper cut-off in which a portion of the intermittency in the smaller simulation is generated by the temporal fluctuations seen in figure 1, while the 64^3 simulation fluctuated very little. Averages of small-scale quantities are very similar in the two simulations.

Although all of the data discussed in detail below was obtained from (2.1) and (2.3)–(2.5), several runs were redone with a different forcing scheme that neglects neither $\mathbf{v}_<.\nabla\mathbf{v}_>$ nor $\mathbf{v}_<.\nabla\mathbf{v}_<$. This was accomplished by splitting off the time evolution of the first band of modes in the spectral code, $k_0 \leqslant k < 2k_0$, from the remainder and time-stepping them according to

$$\frac{\partial \mathbf{u}_k}{\partial t} = -i\alpha P_k \sum_{k'} \mathbf{u}_{k-k'}.\mathbf{k}'\mathbf{u}_{k'}, \tag{2.6}$$

where the sum on k' extends over only the first band. The coupling between the first band and all $k \geqslant 2k_0$ is now reproduced correctly in accordance with the Navier–Stokes equations by the fast Fourier transform. A quantity $\mathbf{S}$, as in (2.1), is not needed. This new algorithm of course decreases the range of dynamically free scales by a factor of 2. We again remark that except for the expected decrease in the overall level of intermittency no qualitative features of the small-scale statistics changed upon going from (2.3) to (2.6).

3. Numerical results

(*a*) *Mean quantities*

For future reference, table 1 contains a digest of the runs to be discussed below. The 32^3 and 64^3 simulations have been run in pairs with a common upper cut-off. The actual maximum wavenumbers differ slightly due to the de-aliasing algorithm (Patterson & Orszag 1971). The information contained in the last incomplete shell is generally discarded. The box size in real space is the inverse of the minimum wavenumber times 2π. The viscosities were chosen identically in corresponding runs while the values of ϵ differ slightly to account for energy dissipated in the first band of the 64^3 simulation which has no counterpart in the smaller code.

Our rather long runs were mandated by the fluctuations we observed in the small-scale data in subsection (*c*) below. Run 1*a* was followed for 54 ($= 120(2E_v)^{\frac{1}{2}}/\pi$) large eddy turnover times or 17 000 time steps. The 64^3 code was necessarily run for shorter times; but, since it contains 8 times as many points, the small-scale statistics are comparable to the 32^3 runs. The first several large eddy-turnover times were neglected in each of the runs to allow the initial conditions to relax.

The mean-square velocity and vorticity are tabulated for only the modes in the spectral code, excluding E_u defined in § 2. Increasing α is expected to decrease the energy in the first few bands while leaving the higher bands unaffected. If the force fluctuates more rapidly, the larger scales will be less able to follow it and extract energy. For some of the longer runs we have done the statistics piecewise to estimate sampling errors. These estimates can be transferred to the shorter runs by scaling with the square root of the integration time.

Three different measures of isotropy are tabulated. The ratio of the trace of the square of the average of S^{ab} to the trace of its square averaged is a measure of whether

	32^3 ($2 \leqslant k \leqslant 31{\cdot}1$, box size $= \pi$)			64^3 ($1 \leqslant k \leqslant 30{\cdot}4$, box size $= 2\pi$)		
Run designation ...	1*a*	2*a*	3*a*	1*b*	2*b*	3*b*
Parameters						
α (equation 2.3))	2	4	2	2	4	4
ϵ	0·578	0·578	0·578	0·6	0·6	0·6
ν	0·01	0·01	0·028	0·01	0·01	0·028
$(\epsilon/\nu^3)^{\frac{1}{4}}$	27·6	27·6	12·7	27·8	27·8	12·9
Running time	120·0	120·0	40·0	20·0	38·0	12·0
Mean-square velocity	2·03 ($\pm$0·05)	1·82 ($\pm$0·07)	1·82	3·48	3·04	2·83
Mean-square vorticity	58·0 ($\pm$0·5)	58·1 ($\pm$1·0)	21·2	60·0	59·1	22·0
Measures of isotropy						
tr $(\overline{S^2})$/tr $(\overline{S^2})$ (equation (2.1))	0·03	0·003	0·04	0·54	0·04	0·18
Components of:						
Mean-square velocity	0·25, 0·34, 0·41	0·37, 0·30, 0·33	0·23, 0·36, 0·41	0·31, 0·50, 0·19	0·34, 0·39, 0·37	0·29, 0·42, 0·29
Mean-square vorticity	0·34, 0·33, 0·33	0·32, 0·35, 0·33	0·34, 0·33, 0·32	0·34, 0·33, 0·33	0·34, 0·33, 0·33	0·36, 0·29, 0·35

TABLE 1. Basic parameters for numerical runs. The rate of energy input and viscosity are denoted by ϵ and ν. Consistent length and time units are used throughout the paper. The uncertainties tabulated for certain quantities from runs 1*a* and 2*a* are an estimate of random errors obtained by recomputing statistics from subsets of the numerical data.

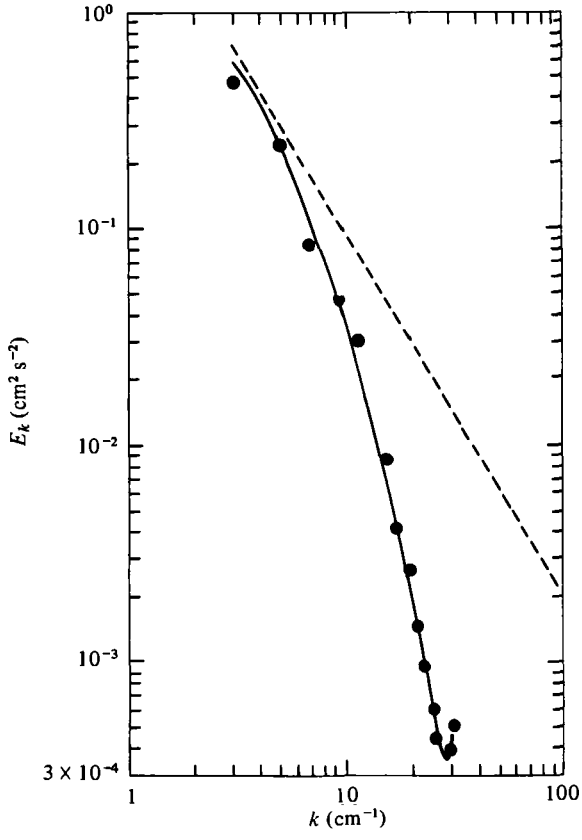

FIGURE 2. The effect of increasing α in (2.3). The continuous curve is the energy spectrum of run $1a$ ($\alpha = 2$), the points are from run $2a$, and the dashed line has a $-\frac{5}{3}$ slope. The energy difference in the first band, $2 \leqslant k < 4$, plotted at $k = 3$ is real.

the forcing modes, $\mathbf{u}_G$, in (2.3) have evolved sufficiently to sample fully their phase space. There is a tendency to use larger values of α in (2.3) than would otherwise be judged optimal for this reason. The only problematical run was $1b$. Here the system seemed to get stuck in a particular configuration that led to very efficient energy transfer between the u and v modes of § 2. Efficient of course means that E_u became quite small while maintaining

$$\sum_k \mathbf{v}_{-k} \cdot \mathbf{S} \cdot \mathbf{v}_k$$

about equal to ϵ. The u modes consequently evolved very slowly. We believe this event to be just a fluctuation and not indicative of any instability in our parametrization of the large scales.

Irrespective of the large-scale anisotropy in run $1b$ we will see that, beyond the first few bands, all the spectra from runs $1b$ and $2b$ agree. Thus, run $1b$ provides a useful illustration of the degree of small-scale universality in isotropic turbulence.

The anisotropy in the small and large wavenumbers in the spectral code is measured by the mean-square velocity and vorticity components normalized to 1. The vorticity is uniformly isotropic even when the large scales are as anisotropic as run $1b$. Although the 64^3 runs give good small-scale statistics, most of the energy resides in the first few

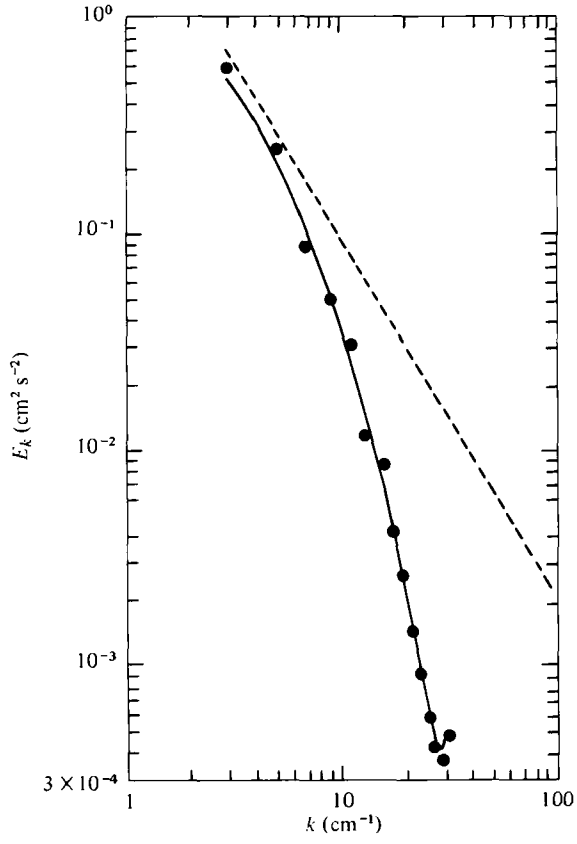

FIGURE 3. Comparison between the energy spectra of run 1*a* (points) and run 1*b* (curve). The first band of wavenumbers, $1 \leqslant k < 2$, from run 1*b* was not plotted, and the remaining bands were added pairwise so as to be comparable with the 32^3 data from run 1*a*.

bands where there are no more modes than in the 32^3 code. The larger box is not wholly compensated by the larger energy attained in the 64^3 simulations, making the isotropy of $\langle v_1^2 \rangle$ more difficult to achieve. Run 1*b* only lasted for 12 large eddy-turnover times of which the first two were excluded from the averaging.

(*b*) *Spectra*

Running averages of seven spectra were maintained for each run in table 1. In addition to the energy there are separate spectra for each of the three terms in the energy and vorticity balance equations, (2.2*a*, *b*), corresponding to input from the force, nonlinear transfer or production, and dissipation. All spectra are actually integrals over wavenumber bands defined as:

$$n \leqslant k < n+1, \quad n = 1, 2, \ldots, 30 \quad \text{for } 64^3 \text{, simulation}$$

$$2n \leqslant k < 2n+2, \quad n = 1, 2, \ldots, 15 \quad \text{for } 32^3 \text{ simulation.}$$

The energy spectra thus have units of cm^{2}s^{-2}. Like-numbered bands contain the same number of modes, though, for a given range of wavenumbers, the 64^3 simulation uses

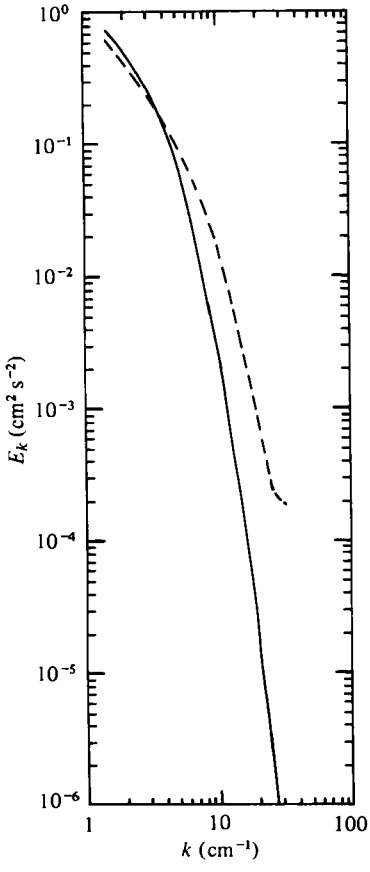

FIGURE 4. Comparison between the energy spectra of run 3*b* (solid line) and run 2*b* (dashed line). The Kolmogorov lengths are respectively 13 and 28.

a denser lattice in k space. When 32^3 and 64^3 data are compared on a single graph, the first band is generally ignored and the remaining bands added pairwise to obtain 14 numbers that then represent the same bands of scales computed by the 32^3 code. The last band is incomplete and generally ignored. For the large scales, the band integrals do not strictly correspond to spectra since the bands are of finite width and the mesh of points in k space is somewhat uneven. Nevertheless, we maintain it is still permissible to compare the two simulations bandwise since the same range of scales is involved.

In figure 2 we show the energy spectra for runs 1*a* and 2*a* along with a line corresponding to a $-\frac{5}{3}$ law. The difference between the first bands is real and is responsible for the difference in energies noted in table 1. All other bands agree to within statistical uncertainties. At least by this crude measure, the small scales are universal with respect to the parameter α. Similar agreement was obtained between runs 1*b* and 2*b*. We use a somewhat larger viscosity than is commonly done to resolve the first derivative flatness (see below). The slight hook at the upper cut-off is a truncation effect that is commonly seen with a purely viscous damping and is not believed to affect lower wavenumbers. It can be removed by any of a number of schemes that attempt to

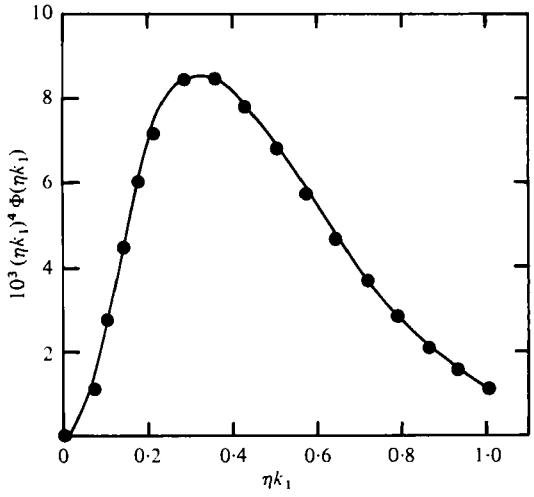

FIGURE 5. Comparison of the dimensionless one-dimensional energy spectrum times $(\eta k_1)^4$ between experiment (Champagne 1978, figure 26, $R_\lambda = 138$) and run 1*b*. The experimental numbers are shown as points. The Kolmogorov length is denoted by η and Φ satisfies

$$\langle u_1^2\rangle/(\epsilon\nu)^{\frac{1}{2}} = \int_0^\infty \Phi(x)\,dx.$$

model the eddy damping due to modes beyond the cut-off (Kraichnan 1976; Siggia & Patterson 1978).

The R_λ computed from just the modes in the spectral code is ~ 35 for the 32^3 and ~ 60 for the 64^3 simulations. The actual R_λ, we estimate, is a factor of $2^{\frac{3}{2}}$ larger because of the exchange of energy between the u and v modes (2.3)–(2.5). The computed level of intermittency is compatible with the larger R_λ.

Of somewhat more interest is a comparison between a 32^3 and 64^3 run in figure 3. The difference between the two runs in the first band, $2 \leqslant k < 4$, is within statistical uncertainties. Higher bands also agree except for a small oscillation in the 32^3 spectrum that we have seen before (Siggia & Patterson 1978) and do not understand. Somewhat better agreement was found between runs 2*a* and 2*b*.

Runs 3*a* and 3*b* are highly dissipative (figure 4). It was necessary to make the Kolmogorov wavenumber, η^{-1}, less than $\frac{1}{2}$ the upper cut-off to fully resolve the second-derivative flatness.

Lastly in this series is a plot in figure 5 of the one-dimensional energy spectra $E_1(k_1)$ times k_1^4 in dimensionless form along with experimental data from a cylinder wake experiment at $R_\lambda = 138$ reported by Champagne (1978). The experiments are virtually R_λ independent in this range, so it doesn't matter that the computation does not reach his R_λ. There are no free or fitted parameters in either theory or experiment. An integral had to be performed on the numerical data to extract the one-dimensional spectra. It was done numerically after fitting the three-dimensional energy spectrum to a continuous function. The one-dimensional spectrum was completely independent of fitting function for $\eta k_1 \lesssim 0{\cdot}55$. To do the integral for larger ηk_1, we chose a fitting function that was plausible for $k \to \infty$, namely

$$E(k) = \frac{a}{k^{\frac{5}{3}}} \exp\,(bk^{\frac{1}{3}} + ck),$$

Run	1*a*	2*a*	3*a*	1*b*	2*b*	3*b*
Forcing	11·9	14·5	6·2	5·8	6·7	4·2
Nonlinearity	65·0	66·2	13·9	70·2	70·4	15·1
Dissipation	77·0	80·8	20·0	76·5	78·3	19·2
Skewness	0·49 (±0·01)	0·49 (±0·02)	0·47	0·50	0·51	0·49

TABLE 2. The three terms in the vorticity-balance equation (2.2*b*) time averaged. The skewness is computed from $S = \frac{6}{7}\sqrt{15}\,\langle\omega_i\boldsymbol{\omega}.\nabla u_i\rangle/\langle\omega^2\rangle^{\frac{3}{2}}$.

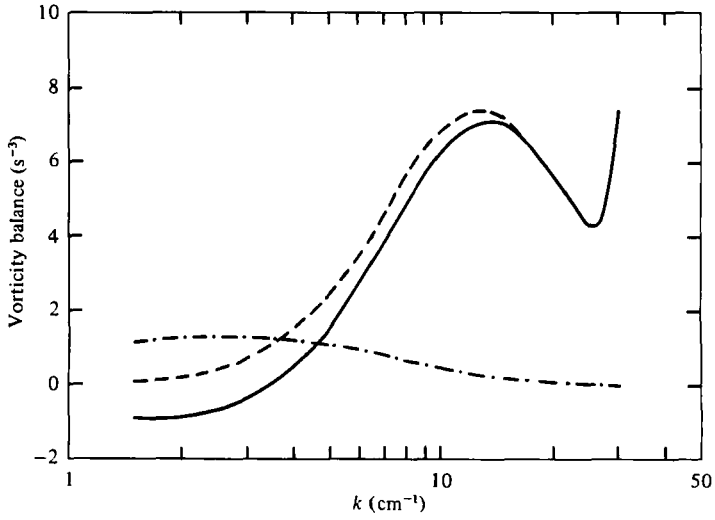

FIGURE 6. Spectra corresponding to the three terms in the vorticity balance equation (2.2*b*) for run 1*b*. The dash-dot, solid, and dashed lines correspond respectively to the forcing, nonlinear production, and the negative of the dissipation. The corresponding spectra from run 2*b* were virtually identical for $k \geqslant 4$.

with a, b, and c free parameters. By fitting to other functions that behaved unphysically for large k we were able to vary the last point in figure 5, $\eta k_1 = 1$, by 50 %. The small unphysical tail in figure 3 at high wavenumbers has no effect on our determination of $E_1(k_1)$.

Monitoring the three terms in the vorticity balance equation (2.2*b*) has proved to be a very useful diagnostic for our simulation (table 2). Several trends are apparent. Increasing α decreases the energy in the first band and increases the ratio of vorticity injected to that produced by the nonlinearity. In all runs with $\nu = 0{\cdot}01$, however, the internally generated vortex stretching is the dominant source of vorticity, which is one reason why we are not concerned about the nonphysical features of (2.1). The vorticity balance equation is indeed well satisfied. The energy equation is almost as well confirmed with the residual discrepancy quantitatively accounted for by the difference in energy between the initial and final times in the average.

The spectra corresponding to the entries in table 2 provide a quantitative measure of the distribution in wavenumber of the forcing and production. The code does not separate the two cubic terms in (2.2*b*) and the net transfer into a band is always included with the production, $\omega^a\boldsymbol{\omega}.\nabla v^a$, when spectra are computed. The overall

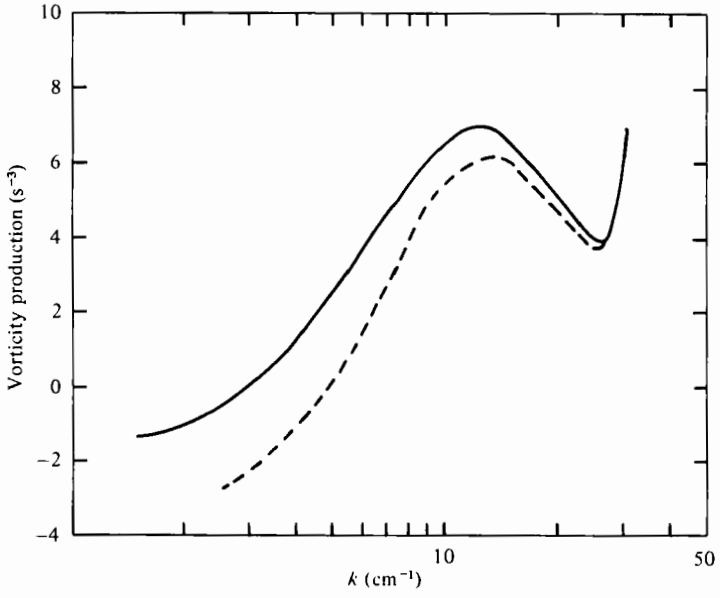

FIGURE 7. Nonlinear vorticity production spectra for a portion of run 1*b* before (solid) and after (dashed) zeroing all modes with $1 \leqslant k < 2$. The integrated production decreases from 69 to 57 (s^{-3}). The change in shape is a useful measure of the range of interaction in wavenumber.

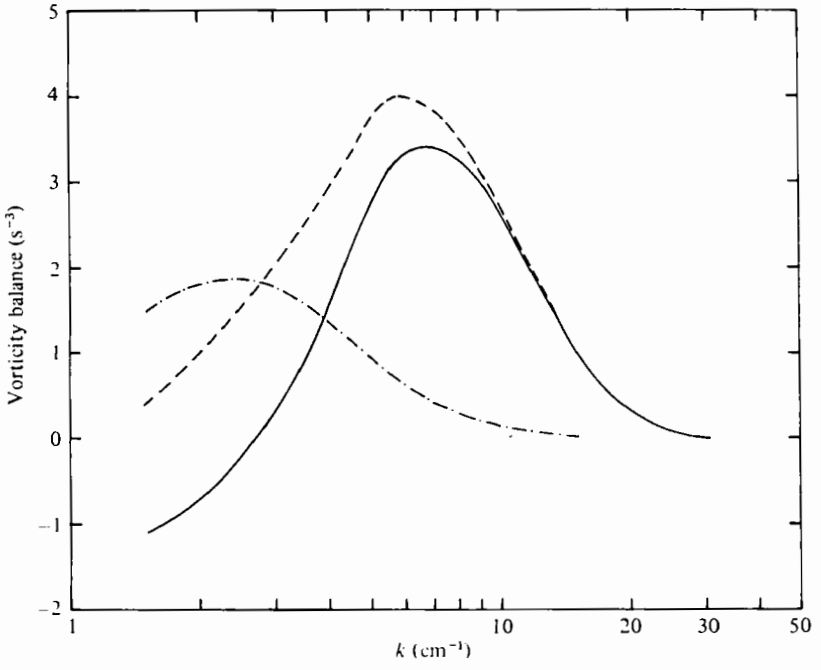

FIGURE 8. Spectra corresponding to the three terms in the vorticity balance equation (2.2*b*) for run 3*b*, following the notation of figure 6.

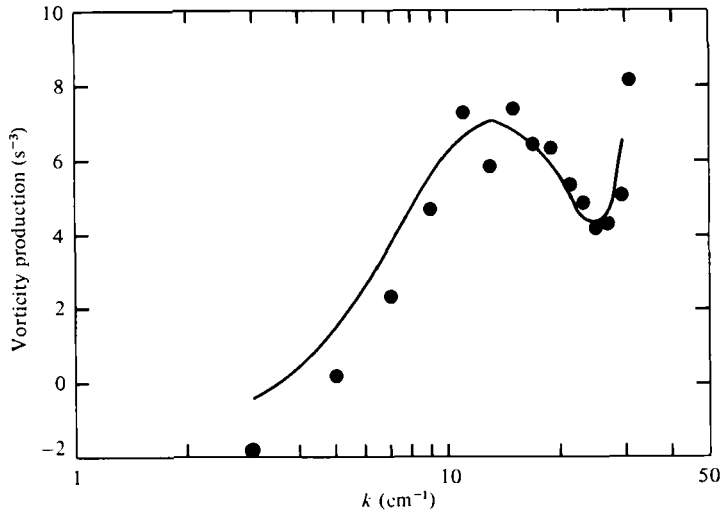

FIGURE 9. The nonlinear vorticity production spectra from run 1*a* (points) and run 1*b* (curve). The first band from the 64^3 run was not plotted.

balance noted above continues to hold band by band. Figure 6 shows the three spectra for run 1*b*. The vorticity produced by the external shear is surprisingly confined to quite small wavenumbers, even though the spectrum falls entirely within the dissipation range. Note that the ratio of forcing to nonlinear transfer or production is the same for the energy and vorticity beyond the first few bands. At a wavenumber of 8 in figure 6, the forcing is only 15 % of the production term. To verify that this is not an artefact of the large scale parametrization, all spectra were recomputed after zeroing the modes in the first band. A comparison is then made between the vorticity production spectra, computed entirely by the spectral code, before and after zeroing the first band, figure 7. One's estimate of the interaction range is unchanged, that is, by $k = 16$ the two curves in figure 7 agree to within 15 %.

Figure 8 is the analogue to figure 6 for run 3*b*. The vorticity dissipation is now fully resolved, while it was not in figure 6. The energy spectrum falls by over 10^6 from the first band to the last in run 3*b* and yet the nonlinearity still dominates the forcing at high wavenumbers.

Figure 9 compares the vorticity production in runs 1*a* and 1*b*. The curious dip in the 32^3 spectrum at $k = 13$ is not an artifact of limited statistics but rather a systematic error we do not understand. The 32^3 calculation falls below run 1*b* at small wavenumbers since the modes $1 \leqslant k < 2$ are missing in the former. The dashed curve in figure 7 (modes $1 \leqslant k < 2$ set to zero) would fit run 1*a* much better and is a more legitimate comparison. The graphs for the total vorticity generation, figure 10, are essentially identical and simply a consequence of similar energy spectra for runs 1*a* and 1*b* in figure 3.

Figure 11 shows the effects of increasing α on the vorticity production. The trend is in accord with what one would infer from the observed changes in the energy spectrum in figure 2.

We had hoped to fix an optimal value of α by comparing only spectral information from the 64^3 and 32^3 simulations. Both the energy in the lower wavenumber bands

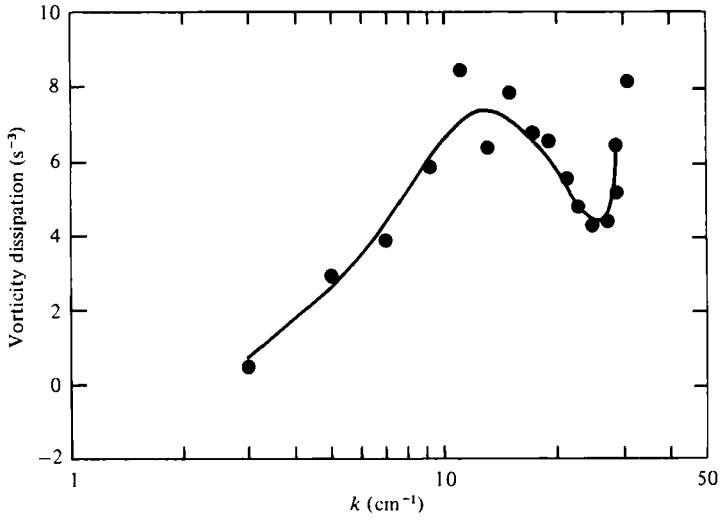

FIGURE 10. Total vorticity production or dissipation spectra for run 1*a* (points) and run 1*b* (curve).

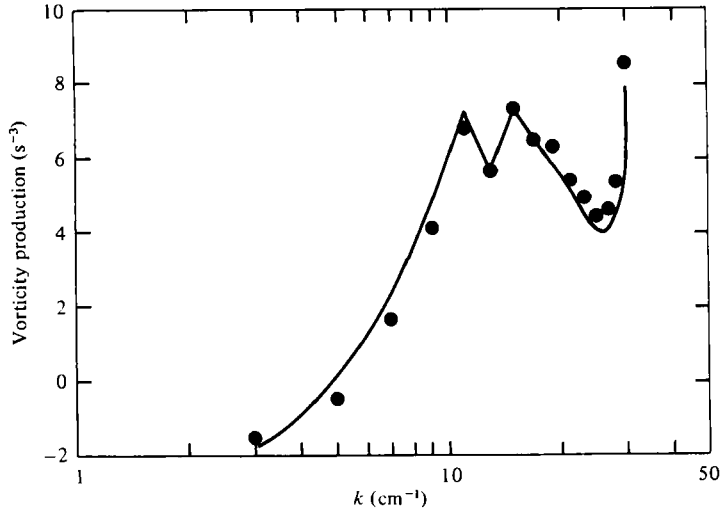

FIGURE 11. The effect of increasing α (2.3) on the nonlinear vorticity production spectra. The curve is run 1*a* ($\alpha = 2$) and the dots run 2*a* ($\alpha = 4$).

and the shape of the vorticity production spectra, depend in a monotonic way on α. When two simulations are run with a common cut-off, the large-scale parameters applied to the 32^3 run ($2 \leqslant k < 32$) model both the forcing applied to the larger code plus the interaction of the first band ($1 \leqslant k < 2$) with the remaining modes. If too large a value of α is used in a 64^3 run, it should be partially compensated, insofar as modes $k \geqslant 2$ are concerned, by the degrees of freedom in the first band. Based on our impressions of how rapidly initial anisotropies disappear in time, we believe that $\alpha = 4$ is rather large, yet we find that the energy between $2 \leqslant k < 4$ from run 2*b* is

0·470 while run 2*a* gave 0·466. For comparison note that run 1*a* gave 0·570. We had hoped 2*a* would have been smaller than it was, implying an optimal α smaller than 4. The analogous data from runs 1*a* and 1*b* were also very close. We have also attempted to fix α by comparing the vorticity production spectra with all modes $1 \leqslant k < 2$ zeroed in the 64^3 data. A value less than 4 is suggested, but we are too unsure about the systematic errors to be certain.

Both a comparison of analogous runs with different values of α (e.g. run 1*a vs.* run 2*a*) as well as between runs with the same α but different resolutions indicates very little sensitivity to this parameter beyond the first few bands. While this suggests a gratifying universality of the small scales, it also frustrates the scheme outlined in § 1 for fixing α and by implication any other parameters one might have introduced into the forcing function.

(*c*) *Higher-order statistics*

(1) *Statistical measures of intermittency*

We were led to run the 32^3 and 64^3 simulations in parallel in order to fix iteratively the parameters modelling the large scales. The most obvious of these is the probability distribution of $\epsilon(t)$ in (2.3). It should thus be necessary for the rate of energy input into a 32^3 simulation to fluctuate if the small scales are to be matched to a 64^3 run at constant ϵ. Again we have not succeeded in fixing the necessary parameters, since unmanageably long runs are required to accumulate sufficiently accurate statistics. A drift in the flatness on a scale of 10 large eddy-turnover times came as a surprise to us and suggests that a rather subtle arrangement of modes is responsible for the strong intermittent bursts we periodically see. It also indirectly suggests rather less local interactions than we inferred from the spectra.

While we have in no sense accomplished the goals set forth in § 1, our simulations, in particular the ability to compare codes of different sizes, have yielded interesting information on the universality of small scales. We can make this claim, even after asserting that our statistics are not good enough to distinguish run 2*a* from 2*b*, for two reasons. The first is that all measures of small-scale intermittency move together. When for instance the flatness, $\langle(\partial u_1/\partial x_1)^4\rangle/\langle(\partial u_1/\partial x_1)^2\rangle^2$, computed from two segments of data agree, so will the $\partial u_2/\partial x_1$ flatness and similar quantities. (This assertion is documented below.) Secondly, a similar correspondence holds between segments of the 32^3 and 64^3 runs. Even though much of the intermittency in the smaller simulation is temporal in origin, in a sense to be made more precise below, the conventional measures of intermittency are very close to the 64^3 run. In the succeeding paragraphs, we will discuss one- and two-point measures of intermittency and at the end display pictorally some of the structures imbedded in the dissipation range.

Higher-order statistics are computed from a history tape on which the velocity field is periodically saved (every 0·4, 0·6 s for the 32^3 and 64^3 data) in the course of the simulation. We think of these data as an experimental tape artificially segmented. Thus to compute a flatness we would form $(\partial u/\partial x)^4$ and $(\partial u/\partial x)^2$ at each time, sum over the lattice and the three equivalent spatial directions, average the various times, and finally take the ratio. For a two-point quantity such $\langle\omega^2(r)\,\omega^2(0)\rangle - \langle\omega^2\rangle^2$, we first did a space and time average of $\langle\omega^2(r)\ \omega^2(0)\rangle$ and $\langle\omega^2\rangle$ separately and then subtracted.

Just as an experimentalist can divide his tape into segments and compute the

flatness within each to estimate fluctuations, we can compute the flatness at each time. For runs $1a$ and $2a$, the time-averaged flatness was appreciably less than the correct flatness computed as the ratio of time-averaged correlations. We thus say that the intermittency was in part temporal. The time average for run $1b$, it will be shown, can be done either on the ratio or on the numerator and denominator separately with similar results. This does not mean there are no fluctuations, though they are less than in the 32^3 runs, but rather that the numerator and denominator of the flatness are sufficiently well correlated to permit interchange of the time average. Artificially blocking the 64^3 data into 8 pieces would give results more like runs $1a$ and $2a$. A comparison between these 32^3 and 64^3 runs is thus of added interest due to the ostensibly different nature of the intermittency.

There are several ways to bring out the intermittency in a numerical simulation. The first is to follow experiment and compute derivative data at a point. This we have done extensively and have got a number of quantities either inaccessible experimentally because of the constraints imposed by the frozen turbulence assumption, or difficult to resolve with conventional hot wires.

Experimentalists have traditionally measured only $\langle(\partial u_1/\partial x_1)^4\rangle$. The flatness is only one component of the general 8-index tensor, $\langle\partial_a u_b \partial_c u_d \partial_e u_f \partial_g u_h\rangle$ which even though all quantities are at the same point provides more than just intensity information about the intermittent regions. The general tensor describes in particular how the vorticity is aligned with respect to the rate of strain and could very easily distinguish a shear from a pure strain or rotation.

Exploiting isotropy and homogeneity greatly reduces the number of invariants necessary to determine the general tensor completely. Rewrite $\partial_a u_b$ as the sum of the rate of strain $e_{ab} = \frac{1}{2}(\partial_a u_b + \partial_b u_a)$ and the vorticity. The general tensor breaks into three pieces that can be distinguished by the number of factors of $\boldsymbol{\omega}$. Isotropy implies that $\langle\omega_a\omega_b\omega_c\omega_d\rangle$ is determined by a single scalar, e.g. $\langle\omega^2\omega^2\rangle$. Similarly, $\langle\omega\omega ee\rangle$ (dropping indices) can be recovered from the two scalars one can form from the indicated fields, namely $\langle\omega^2 \operatorname{tr} e^2\rangle$ and $\langle\boldsymbol{\omega}.\mathbf{e}.\mathbf{e}.\boldsymbol{\omega}\rangle$. The exact tensor form will be given elsewhere. Finally for $\langle eeee\rangle$, Betchov (1956) has shown there is only one scalar invariant either $\langle(\operatorname{tr}(e^2)^2\rangle$ or $\langle\operatorname{tr}(e^4)\rangle$ $(= 105\langle(\partial u_1/\partial x_1)^4\rangle/8)$, provided one remembers $\operatorname{tr}(\mathbf{e}) = 0$. Thus using only isotropy and incompressibility we find four scalars determine the general 8-index tensor. It may be shown that homogeneity does not provide any further relations among the four scalars (Siggia 1981). All four are tabulated below. Our reduction scheme has also been applied to higher-order tensors.

In any calculation of a higher-order correlation function from numerical data one has to investigate to what extent modes beyond the resolution of the simulation would alter the result. The simplest check is just to zero successively the first and last octaves of data, recompute all correlations and verify changes are small. This we have done. It should also be verified that aliasing is unimportant; namely that the lattice sum of the product of three or more fields equals the corresponding sum over the product of the Fourier-transformed fields with the restriction that the wavenumbers add to zero and not zero modulo the box size. A spectrum slightly steeper than figure 3 is required optimally to resolve, for both small and large wavenumbers, the tensor $\langle(\partial u)^4\rangle$.

Among the other ways of displaying the intermittency of our simulation are band-limited quantities and structure functions. Both provide measures of how fluctuations

Run (time)	Gaussian	1*a* (4–40)	1*a* (40–80)	1*a* (80–120)	2*a* (4–40)	2*a* (40–80)	2*a* (80–120)	1*b*	2*b*
$\langle(\partial u_1/\partial x_1)^4\rangle$ (*R*)	3	4·66	3·68	4·30	6·38	4·47	5·02	4·57	5·52
(*k*)	?	4·45	3·76	4·09	6·00	4·32	4·62	4·43	4·74
(*T*)	3	3·82	3·30	3·80	4·40	3·88	4·10	4·54	4·35
$\langle(\omega^2)^2\rangle$	$\frac{5}{3}$	3·25	2·86	3·10	4·00	3·23	3·41	3·70	3·91
$\langle\omega^2 \operatorname{tr}(e^2)\rangle$	1	2·07	1·77	1·92	2·49	1·98	2·09	2·01	2·42
$3\langle(\boldsymbol{\omega}.\mathbf{e}.\boldsymbol{\omega}\rangle$	1	0·76	0·80	0·87	0·93	0·79	0·85	0·81	1·10
$\langle(\partial^2 u_1/\partial x_1^2)^4\rangle$ (*R*)	3	7·61	6·50	7·56	10·0	7·16	8·01	7·88	15·6
(*k*)	?	5·55	5·02	5·86	7·58	5·38	6·06	5·65	8·47
$\langle[(\partial^2 u_1/\partial x_1^2]\,\partial^2 u_1/\partial x_2^2)^2\rangle$	1	4·30	2·91	3·95	4·30	3·16	3·59	3·54	4·58
$\langle(\partial^2 u_1/\partial x_2^2)^4\rangle$	3	15·0	12·2	13·0	16·4	12·2	14·0	11·9	20·3

TABLE 3. Selected higher-order derivative statistics for runs 1 and 2 and a hypothetical system prepared with Gaussian random velocity modes. All correlations are normalized by the corresponding quadratic means as explained in the text. Correlations marked as (*R*) or unmarked are summed in real space, averaged in time, and then normalized. The spatial average is de-aliased prior to time averaging and normalizing in quantities marked with (*k*). A correlation for which the normalization follows the spatial average but precedes the time average is denoted by (*T*).

grow with decreasing scale size. Structure functions are difficult to interpret when the underlying data do not scale and can show spurious changes when the spatial separation approaches several lattice constants (Siggia & Patterson 1978). Similar comments would apply to a band-averaged flatness which we have only computed as a resolution check.

Next in the hierarchy of correlation functions are those at two points which provide information on the size of intermittent regions. In this category we have computed only $\langle\omega^2(\mathbf{r})\,\omega^2(0)\rangle$ as a function of $|\mathbf{r}|$ and again with the direction of $\mathbf{r}$ coinciding with each of the three orthogonal axes with respect to which the matrix $\mathbf{S}$ is diagonal. In principle, a two-point function provides information on the geometry of the active regions as well as their size, but such distinctions are rather subtle and model dependent (Kuo & Corrsin 1972). To characterize vortical structures definitively as tubes or sheets for instance with correlation functions, one has either to compute three-point averages or conditionally sample $\langle\omega^2(\mathbf{r})\,\omega^2(0)\rangle$ with $\mathbf{r}$ either parallel or perpendicular to the local vorticity vector. A tube with the vorticity internally aligned would give a very different correlation length depending on the relative orientation of $\boldsymbol{\omega}$ and $\mathbf{r}$. Either of these alternatives is cumbersome to implement numerically so we have simply made three-dimensional perspective plots of the surfaces of regions of high ω^2 as well as directly plotting the field, $\boldsymbol{\omega}$, at selected points. What appears is quite dramatic, although one's assessment of statistics as to what is a tube, a sheet, and a ribbon will remain somewhat subjective until more elaborate correlation functions are computed.

(2) *One-point statistics*

Table 3 is a summary of the one-point higher-order statistics. The 32^3 data are broken into three segments to give an impression of the magnitude of the fluctuations over quite long time intervals ($\sim$ 16 large eddy turnovers). The first derivative flatness is an average of $\langle(\partial u_i/\partial x_i)^4\rangle$ in the x, y, and z directions normalized by $(\langle\omega^2\rangle/15)^2$.

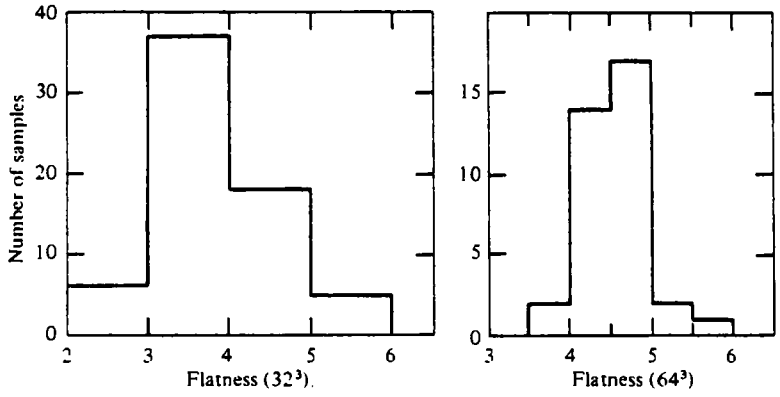

FIGURE 12. Histograms of the instantaneous, though volume-averaged, flatness factors from run 1*a* (T = 4–40) and run 1*b*. The 64^3 bins are half the width of the 32^3 bins.

The isotropy condition $\langle\omega^2\rangle/\langle\mathrm{tr}\,(e^2)\rangle = 2$ was verified to about one per cent. Isotropy was not invoked to normalize the second-derivative flatness factors. Thus

$$F(\partial^2 u_1/\partial x_2^2) = \frac{3\sum_{i=1}^{3}(\partial^2 u_i/\partial x_{i+1}^2)^4}{(\sum_{i=1}^{3}(\partial^2 u_i/\partial x_{i+1}^2)^2)^2},$$

where $x_4 = x_1$.

The three different values of flatness provide a good measure of aliasing or resolution (k *vs.* R), and the amount of temporal intermittency (R *vs.* T), for any of the fourth-order single-derivative correlations. Statistics were recomputed for a portion of run 1*b* after zeroing successively all modes with $k < 2$ and then $k \geqslant 24$. Normalized by its untruncated value, $\langle(\partial u_1/\partial x_1)^4\rangle$ becomes 0·95 and 0·86 in the two cases considered. The flatness of $\partial u_1/\partial x_1$ varies by somewhat less, from 4·5 to 4·8 and 4·2 respectively. Figure 12 contains histograms of the flatness computed timewise for the first segment of run 1*a* and all of run 1*b*. Three separate values of $\langle(\omega^2)^2\rangle$ (R, k, and T) were also computed and follow the flatness data. The flatness factors of the second-order derivatives are clearly aliased and cannot be compared with experiment. Nevertheless we maintain it is legitimate to compare the 32^3 and 64^3 simulations with the aliasing since they should behave identically at high wavenumbers.

The extent of the temporal fluctuations in the flatness and other high-order quantities came as a surprise and prevents us from reporting very precise averages. It is quite interesting to compare individual data segments, for instance run 1*a* ($T = 4-40$, $T = 80-120$), and 2*a* ($T = 40-80$) in table 3. All the one-point measures of intermittency move together, which implies some degree of uniformity in the active regions. It provides evidence that the intermittency can be parametrized without introducing complicated phase variables that would couple preferentially to one of the fourth-order invariants say.

A tolerable similarity also exists between run 1*a* ($T = 4-40$) and 1*b*. This is of some interest because the intermittency in the 32^3 run is largely temporal while the three flatness values for the 64^3 run all agree. Part of the intermittency in run 2*b* is also temporal owing to the exchange of energy between the **u** and **v** modes in (2.2)–(2.5), figure 1. Its one-point derivative statistics therefore exceed those of run 1*b*.

The two quadratic invariants that involve the vorticity and rate of strain merit

Run		3*a*	3*b*
$\langle(\partial^2 u_1/\partial x_1^2)^4\rangle$	(R)	9·5	9·3
	(k)	8·8	9·4
	(T)	5·5	9·3
$\langle(\partial^2 u_1/\partial x_2^2)^4\rangle$		10·7	10·8
$\langle(\partial^2 u_1/\partial x_1^2)^2(\partial^2 u_1/\partial x_2^2)^2\rangle$		3·9	3·5

TABLE 4. The normalized second-derivative flatness factors following the notation of table 3. Resolution errors are estimated in the text.

comment. The first, $\langle\omega^2 \operatorname{tr}(e^2)\rangle$, seems to move with the flatness and exceeds its Gaussian value. It represents a better correlation between vorticity and rate of strain than we found previously (Siggia & Patterson 1978), which may be attributable to the higher R_λ. The other invariant, $\langle\boldsymbol{\omega}.\mathbf{e}.\mathbf{e}.\boldsymbol{\omega}\rangle$, falls below its Gaussian value contrary to one's immediate expectations based on vortex stretching. On average $\det(\mathbf{e}) < 0$, so if we work in co-ordinates that diagonalize e_{ab} and assume $e_{33} < 0$ we arrive at $\boldsymbol{\omega}.\mathbf{e}.\mathbf{e}.\boldsymbol{\omega} = \omega_1^2 e_{11}^2 + \omega_2^2 e_{22}^2 + \omega_3^2(e_{11}+e_{22})^2$. The simplest representation of the correlation between $\mathbf{e}$ and $\boldsymbol{\omega}$ is $\omega_i \sim e^{\tau e_{ii}}$ with τ a positive free parameter. The correlation $\langle\boldsymbol{\omega}.\mathbf{e}.\mathbf{e}.\boldsymbol{\omega}\rangle$ first decreases and then increases as τ increases from zero. Note that if the intermittent regions were pure shears, $\langle\boldsymbol{\omega}.\mathbf{e}.\mathbf{e}.\boldsymbol{\omega}\rangle$ would be zero.

Table 4 collects all the high-viscosity data from runs 3*a* and 3*b*. The first-derivative flatness and related quantities are not reproduced since they come largely from the first few bands in wavenumber and are not adequately resolved. In particular, when modes $1 \leqslant k < 2$ were zeroed in run 3*b*, $\langle(\partial u_1/\partial x_1)^4\rangle$ changed from 17 to 9. Temporal fluctuations in first-derivative quantities are also a problem since fewer modes are contributing than in runs 1*a* and 2*a*.

The second-derivative flatness factors are not aliased, but a second estimate of the resolution by zeroing high wavenumbers indicates we should have run with a larger viscosity. When $\Sigma_i\langle(\partial^2 u_i/\partial x_i^2)^4\rangle$ was recomputed from a portion of the data of run 3*b* after zeroing all modes with $k < 2$ and then with $k \geqslant 16$, it changed from 1·00 to 0·97 and 0·64 respectively in rescaled units. The latter two numbers for $\Sigma_i\langle(\partial^2 u_i/\partial x_{i+1}^2)^4\rangle$ were 0·94 and 0·77. The flatness factors of $\partial^2 u_i/\partial x_i^2$ and $\partial^2 u_i/\partial x_{i+1}^2$ changed from 9·4 and 10·3 to 7·0 and 8·7 after zeroing modes with $k \geqslant 16$.

Kuo & Corrsin (1971) measured a second-derivative flatness of 5 at $R_\lambda \sim 30$, whereas we find a value of order 9 at an $R_\lambda \sim 28$ based on the modes in the spectral code. This is one reason why we believe that our forcing algorithm has effectively boosted the Reynolds' number from what could be obtained from the unforced spectral code. The agreement between runs 3*a* and 3*b* seems to preclude that a single rare event has occurred, and we also recomputed the flatness factors from a portion of run 3*b* to check fluctuations. The resolution errors mentioned above suggest that if the upper wavenumber cut-off were increased to 64 the flatness might increase by 10–20 %, but R_λ would not change since the dissipation is fully resolved.

To lend further support to our unexpectedly large second-derivative flatness we repeated run 3*b* with a slightly larger viscosity, and a longer integration time. We also modified the forcing algorithm so as to use the first band to drive the remaining spectral modes as discussed at the end of § 2. The flatness factors of $\partial^2 u_i/\partial x_i^2$ and $\partial^2 u_i/\partial x_{i+1}^2$ were 7·32 and 10·9. They decreased to 7·00 and 10·8 respectively after

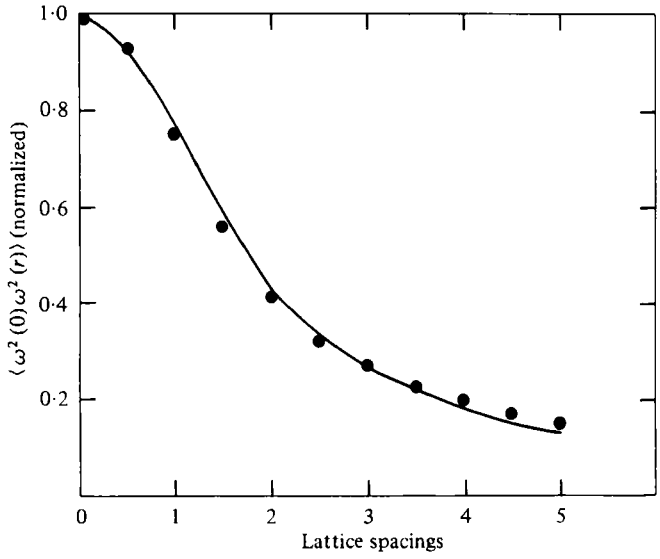

FIGURE 13. $(\langle\omega^2(0)\omega^2(r)\rangle - \langle\omega^2\rangle^2)/(\langle\omega^2\omega^2\rangle - \langle\omega^2\rangle^2)$ for run 1*b* (curve) and run 1*a* (points).

zeroing modes with $k \geqslant 22$. Aliased and de-aliased quantities also agree. The resolution is now unquestionably adequate yet the flatness still exceeds experiment.

Although the results are quite crude, we have conditionally sampled the 32^3 data from runs 1*a* and 2*a* by scanning the various normalized correlation functions averaged over the lattice at a fixed time. A large flatness is marginally associated with a large skewness. It is also found that, when the small-scale structures are sheets and the flatness is large, $\langle\boldsymbol{\omega}.\mathbf{e}.\mathbf{e}.\boldsymbol{\omega}\rangle$ is suppressed uniformly below its timewise average while $\langle\omega^2\omega^2\rangle$ is essentially the same as the ensemble average. When tubes are the dominant structure, $\langle\omega^2\omega^2\rangle$ is enhanced while $\langle\boldsymbol{\omega}.\mathbf{e}.\mathbf{e}.\boldsymbol{\omega}\rangle$ is unaffected.

(3) *Multipoint statistics*

Figure 13 shows the two-point correlation function $\langle\omega^2(0)\omega^2(r)\rangle/\langle\omega^2\rangle^2 - 1$, scaled to bring out the correlation length of the high-vorticity regions. It contains no hint of the rather extended (12–30 lattice spacings) vortical structures actually present. A conditional sample of only the times showing the most extended structures would not appreciably change figure 13.

The correlation between the eigenvalues and directions of S_{ab} in (2.3)–(2.5) and the small-scale vorticity was also examined. The correlation $\langle\omega^2(0)\omega^2(r)\rangle$ was redetermined with the direction of r coinciding successively with the three eigendirections of S_{ab} at each time. The correlation length along the stretching direction is about 50 % larger than the length determined for the principal contracting direction. There was no obvious correlation between det (**S**) and the shape of the small-scale vortical structures. This is probably a consequence of the locality in wavenumber of the external forcing, figure 6, and the failure of (2.1) to reproduce the correct linearized vortex-stretching equations with respect to **S**.

The three-dimensional perspective plots, figures 14–19, that conclude this section are an attempt to provide a sample, biased in favour of the more extended structures,

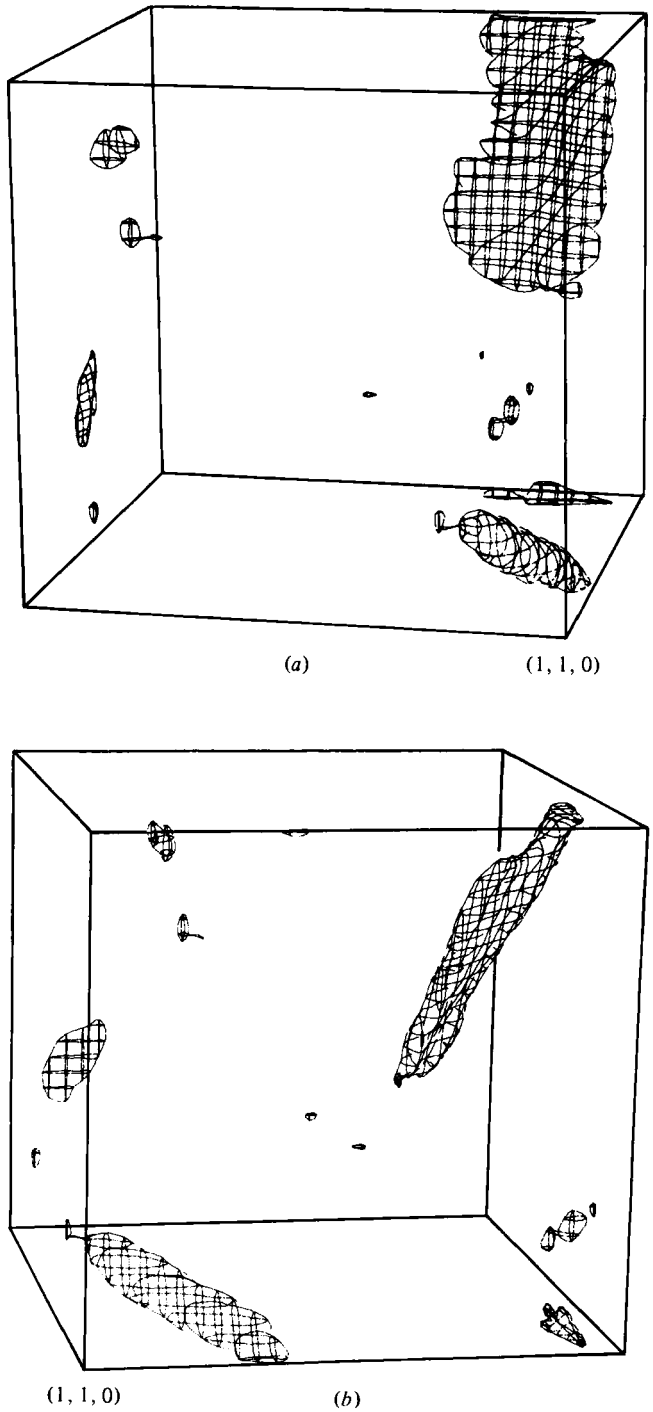

FIGURE 14. Two views of a vortex sheet from run $2a$. The flatness is 4·90. The perspective adopted corresponds to an observer in the first quadrant, i.e. where x, y, z are all positive. The origin is in the back of the box and the lower front corner, (1, 1, 0), is marked in units of 2π.

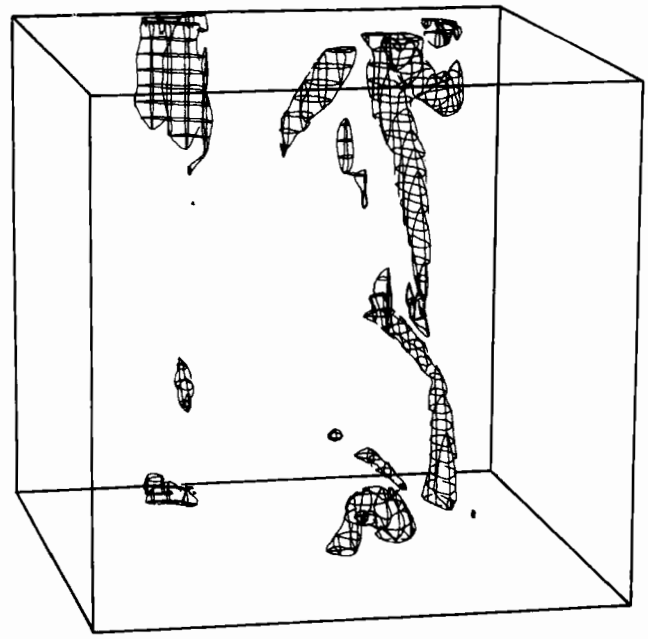

(1, 1, 0) (*a*)

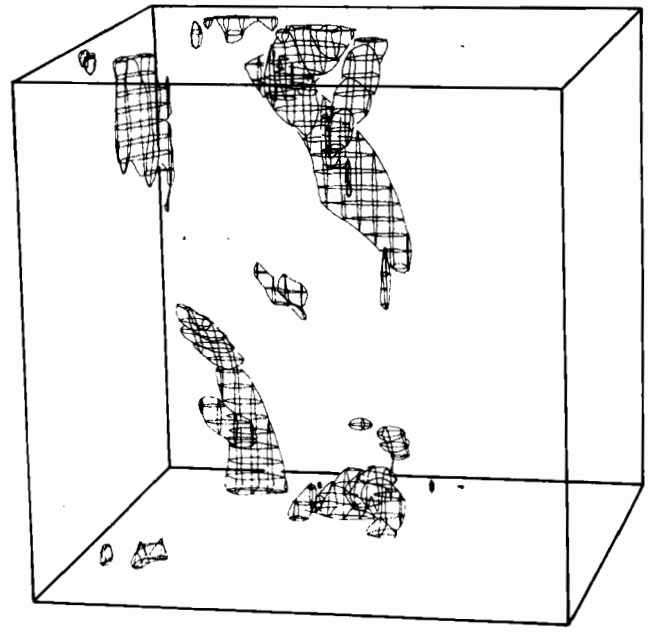

(*b*) (1, 1, 0)

FIGURE 15. Two views of a vortex ribbon that extends through the computational box (run 1*a*). The flatness is 3·23 or nearly Gaussian.

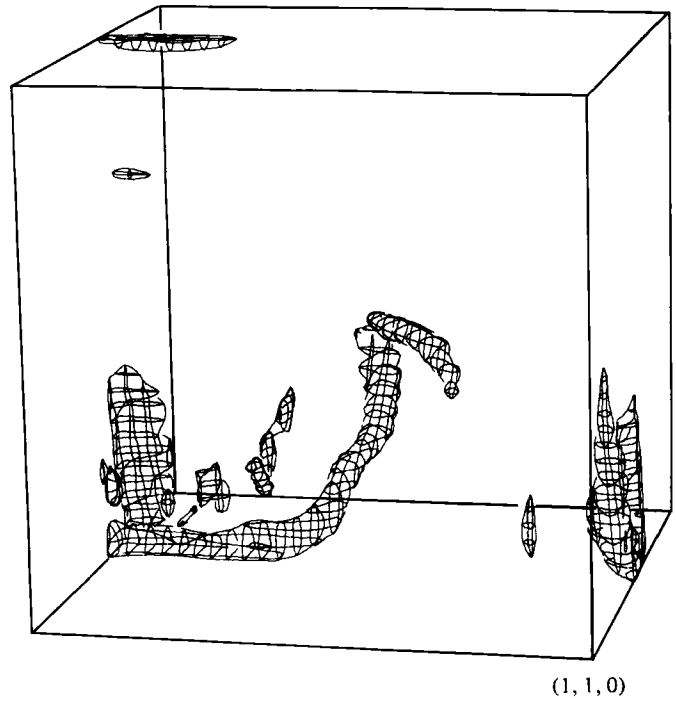

FIGURE 16. A vortex tube from run 1*a*. The flatness is 5·24. A vortex sheet, which is not very well visualized from this angle, extends through the $y = 0$ plane.

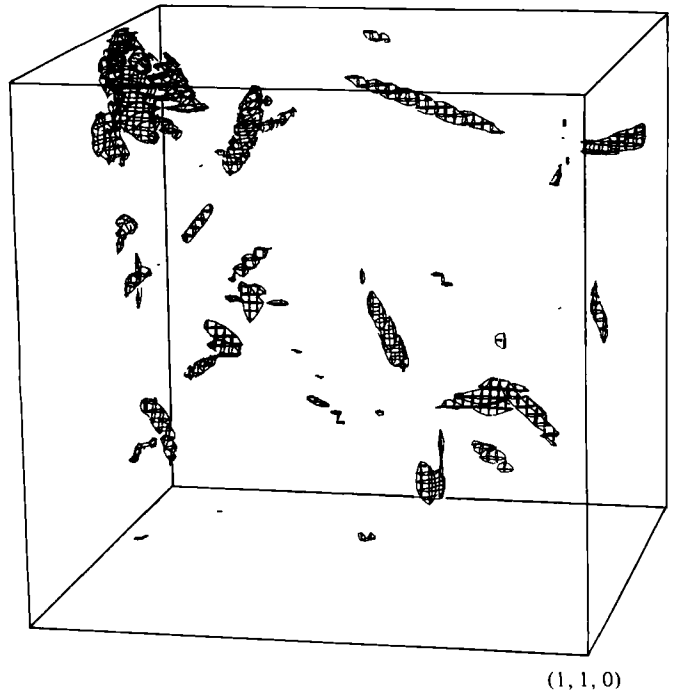

FIGURE 17. Structures present at the time for which the highest flatness, 5·53, was computed from run 1*b*.

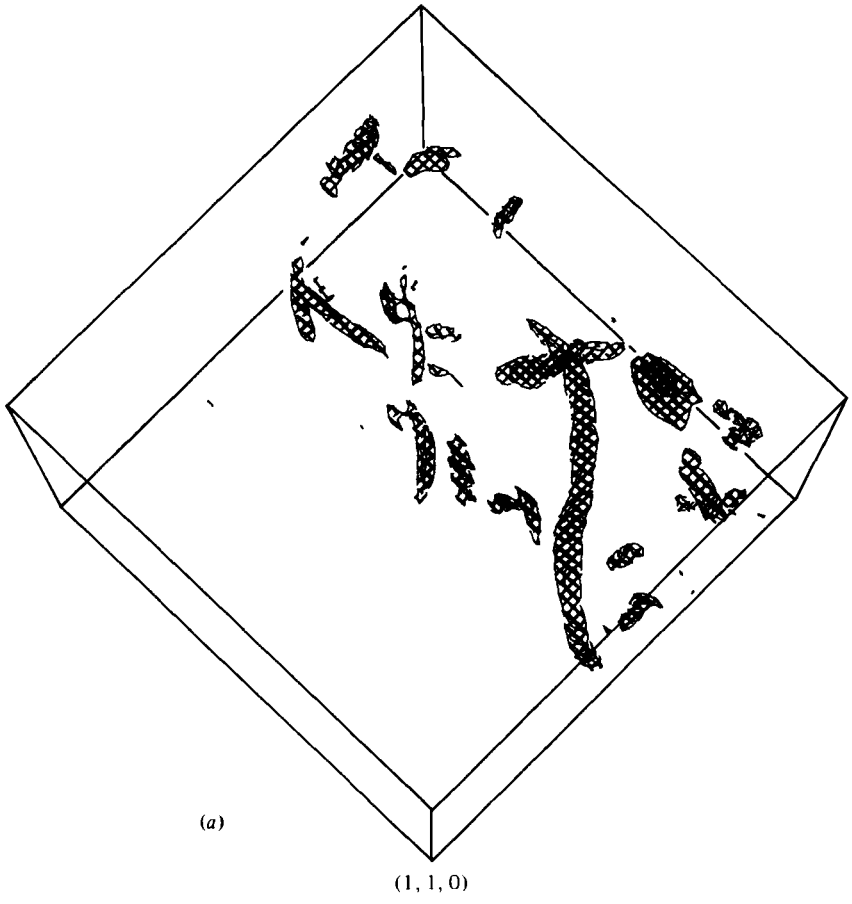

FIGURE 18. Two views of an unusually long and persistent vortex tube from run 1*b*. The flatness is 4·28.

from the thousand or so pictures we have. Figure 17 is perhaps the most typical as regards the size of the vortical structures. It is very difficult to program a computer to recognize arbitrary three-dimensional shapes, so we can do no more here than record our impressions after surveying the entire set of pictures. The contouring algorithm bounds all regions within which the field being plotted, usually ω^2, exceeds some value. We set this value so that the enclosed volume was respectively 0·3 % and 1 % of the total for the 64^3 and 32^3 simulations. These numbers were chosen for aesthetic reasons to optimize the visibility of the structures. It was verified that a tube's length or a vortex sheet's area were only slightly affected by changing the volume fraction enclosed. Projections of the three-dimensional data onto the $x, y, z = 0$ planes were regularly made to facilitate estimates of linear dimensions.

We have seen many examples of vortex tubes and sheets, as well as blobs, with only a tenuous correlation between a large extended structure and a high skewness or flatness (compare figures 15 and 16 or 17 and 18). We have seen that the matrix **S** does not correlate with the geometry of the dissipation range structures but we have un-

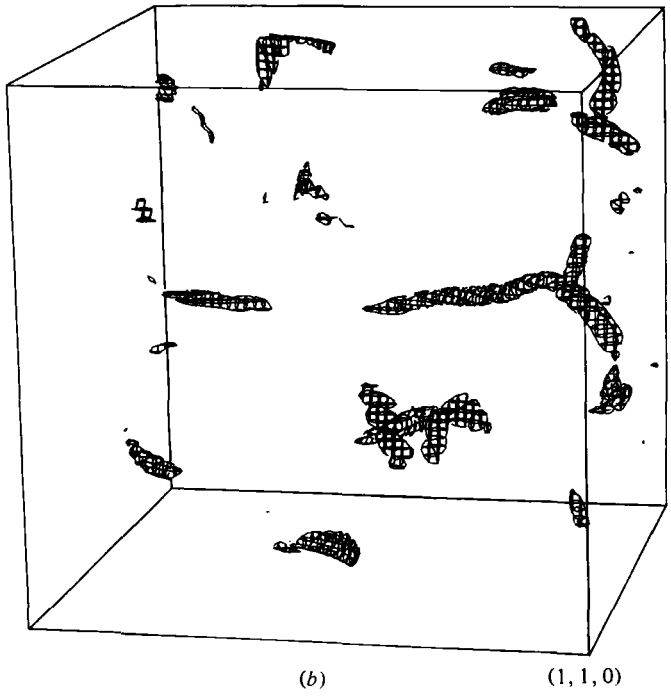

FIGURE 18(*b*). For legend see p. 400.

fortunately not examined the correlation with the rate of strain generated in the lower bands. Redoing the graphics after zeroing all modes with $k < 2$ changes nothing.

An appreciable fraction of our three-dimensional data was regraphed to bring out the direction of the vorticity, figure 19. Starting at each of a random sample of points that fell within the previously drawn surfaces bounding the regions of high vorticity; a line segment was drawn in perspective parallel to $\boldsymbol{\omega}$. Its length was scaled with $|\boldsymbol{\omega}|$. The vorticity vector was invariably parallel to the axes of the vortex tubes and in the plane of the vortex sheets.

We believe that our 64^3 simulation fully resolves the spatial extent of the dissipation range vortical structures present at these Reynolds numbers. We have never seen a tube or sheet larger than half of the 64^3 box, while occasionally a tube was seen in the 32^3 simulation that ran entirely through the box (figures 15–16). Recall that the 32^3 and 64^3 codes were scaled to have the same lattice spacing. Thus, doubling the box size does not double the large dimension of the structures, implying that it is not box limited.

Extended structures, however, do tend to persist longer in the 64^3 box. Exact tube and sheet solutions to the Navier–Stokes equations are known in which vortex stretching balances diffusion (Saffman 1968). Their stability in different environments has not been examined to our knowledge. We conjecture that stability limits their large dimension while their direction and shape are correlated with the rate of strain produced by the large scales. These evolve more slowly in the larger box, implying greater persistence for the underlying structures (figure 20). Figure 21 confirms conventional

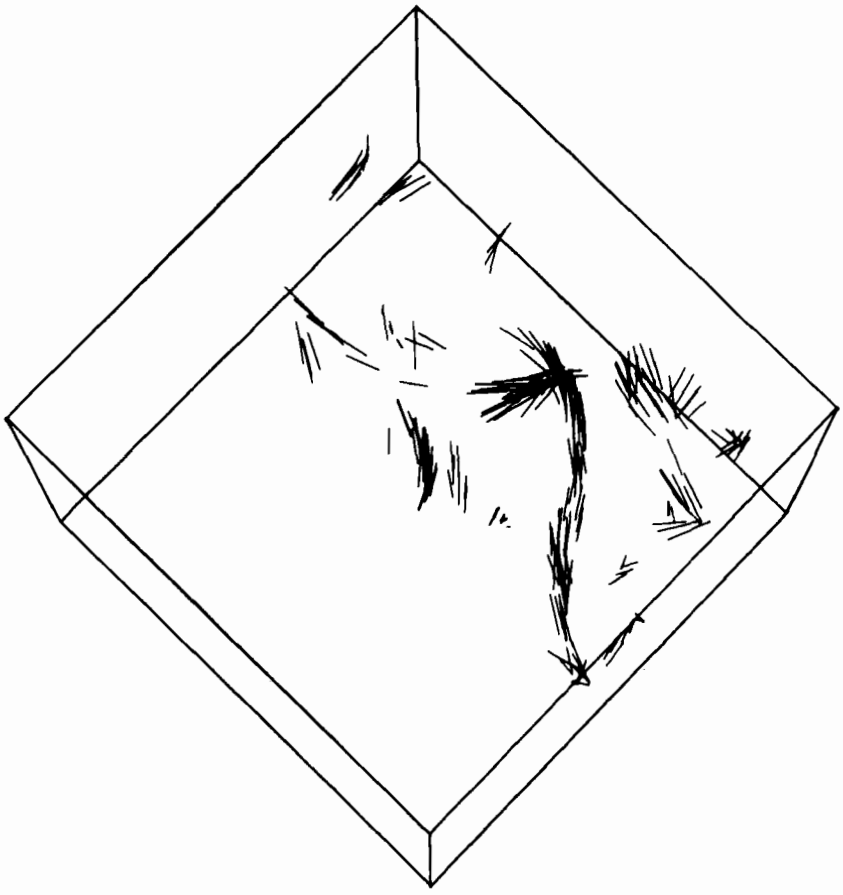

FIGURE 19. A replot of figure 18 (*a*) showing the direction of ω within the vortex structures. Each line segment begins at a point within the structure and its length is proportional to $|\omega|$.

wisdom that structures are most apparent in vorticity plots and do not show up as well in the longitudinal derivative or dissipation.

4. Conclusion

We have numerically achieved a level of intermittency comparable to the early Batchelor & Townsend (1949) experiments by means of a direct spectral simulation without resort to subgrid modelling. Our flows are statistically homogeneous and isotropic. At these low Reynolds numbers, derivative statistics are the best diagnostic of intermittency and a rather extensive set have been calculated. The locality in wavenumber of the external forcing suggests that, from whatever imperfections the large-scale parametrization suffers, the small scales will not be appreciably biased. We also endeavoured to ascertain where in dimensionless wavenumber ηk ($\eta^{-1} = (\epsilon/\nu^3)^{\frac{1}{4}}$) various derivative statistics were determined and then adjusted the spectral shape

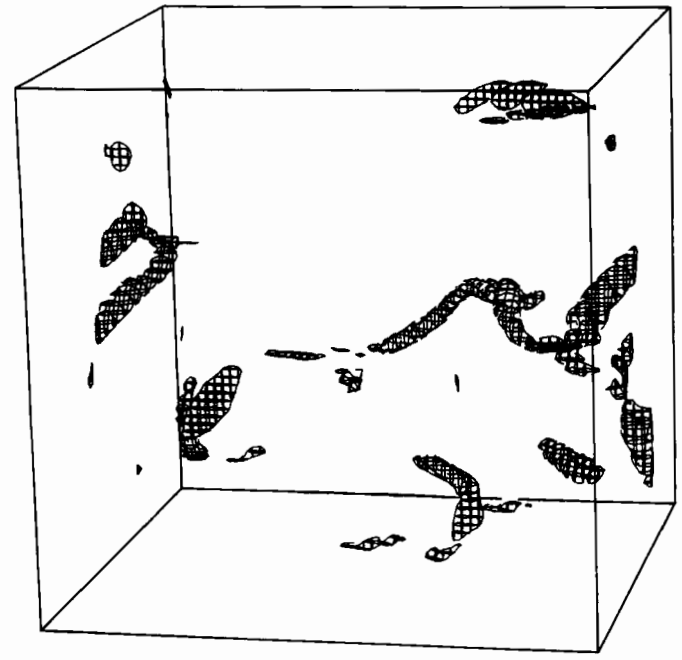

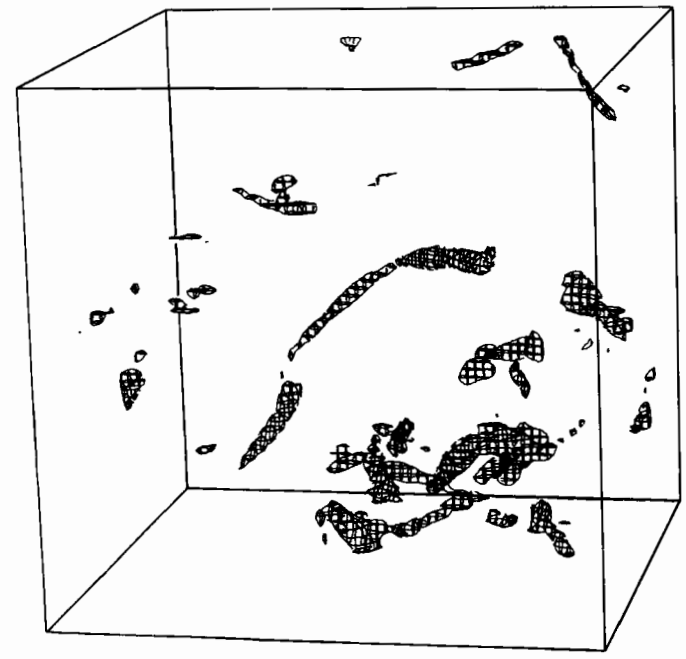

FIGURE 20. A continuation of figure 18 showing the same structure at a time 0·8 and 1·6 (s^{-1}) later. Consult table 1 for more physical units. The flatness factors are 4·69 and 4·65.

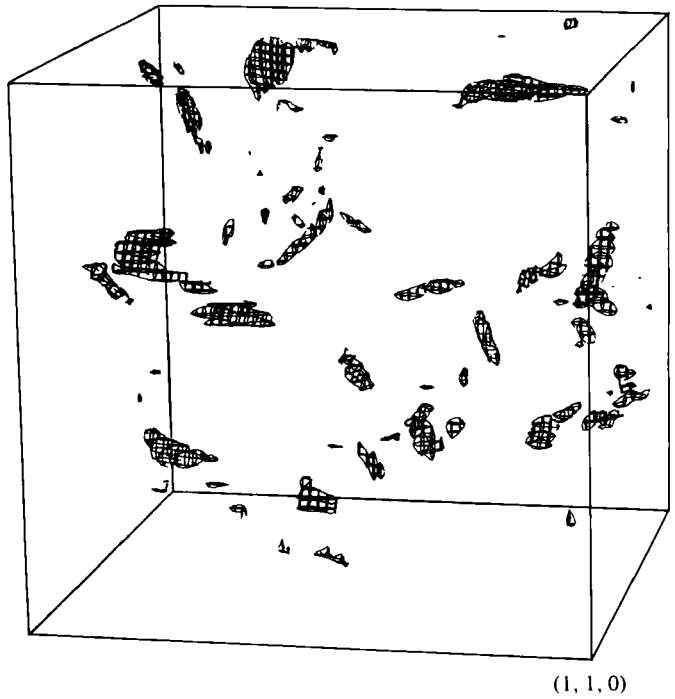

FIGURE 21. A plot of $\Sigma_{i=1}^{3}(\partial u_i/\partial x_i)^2$ at the same time as figure 18. The prominent vortex tube is no longer apparent but the vortex sheet perpendicular to the plane $z = 2\pi$ is nicely reproduced.

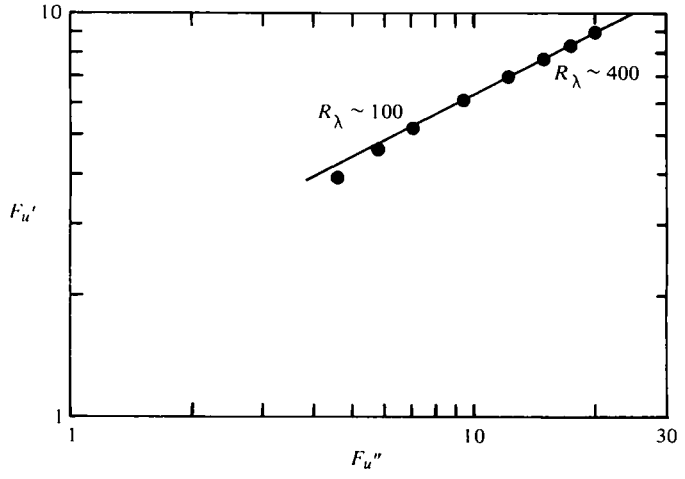

FIGURE 22. Flatness of $\partial u_1/\partial x_1$, against the flatness of $\partial^2 u_1/\partial x_1^2$, from Kuo & Corrsin (1971). The points counting from the left correspond to $R_\lambda = 20$, 50 and 100–600 in units of 100. The line has a slope of 0·50.

to resolve them. The comparison between the 32^3 and 64^3 simulations, scaled to the same lattice spacing, was a useful check on the quality of both.

Considerable interesting information remains to be extracted from our data. The interaction between different scales was not studied and it would be interesting to see in some detail how the vortex structures are generated.

The current state of our knowledge about universality in the small scales of fully developed turbulence is aptly characterized by figure 13 of Kuo & Corrsin (1971) and comparable plots in Van Atta & Antonia (1980) of the first-derivative flatness and skewness. The scatter among different experiments is immense and, we believe, largely due to uncontrolled and unreported systematic errors rather than non-universal behaviour in the small scales. Sampling errors may also have been an unexpected source of scatter in view of the rather long integration times we found necessary for statistics to settle down. A second problem experimentally is the non-universality of R_λ and the difficulty of determining it in the atmospheric boundary layer.

The values of $S/F^{\frac{3}{2}}$ in table 3 of Champagne (1978) are thus of considerable interest since they are constant from $R_\lambda = 182$ to $R_\lambda \sim 13000$. This is rather unexpected since the most one might have hoped *a priori* is a universal curve of F *vs.* S with scaling only at large R_λ. Unfortunately, Champagne has only four experimental points. Our value of $S/F^{\frac{3}{2}}$ is $0{\cdot}27 \pm 0{\cdot}02$ versus Champagne's 0·25. The numerical skewness has always tended to be somewhat larger than experiment.

While invoking some, presumably Gaussian, experimental noise could account for a low skewness, finite wire effects are possibly also at fault, particularly in laboratory experiments. Wire-length corrections can be made rather convincingly for spectra (Wyngaard 1968, 1969, 1971), but to the best of our knowledge higher-order statistics are never corrected. By zeroing high-wavenumber bands, we estimate that to get better than 10 % accuracy at $R_\lambda \lesssim 100$, all scales out to $1{\cdot}2/\eta$ for the first-derivative flatness and $3{\cdot}0/\eta$ for the second-derivative flatness should be completely resolved in length and frequency. At higher R_λ, fluctuations may develop in the inertial range that push the instantaneous η^{-1} well beyond its average value. We hope to simulate numerically a finite probe and pass it through our data to quantify the wire-length errors better.

To pursue somewhat further the question of small-scale universality with existing data, we have replotted in figure 22 the second-derivative flatness found by Kuo & Corrsin (1971) against the first-derivative flatness. A fair straight line again results with a slope near the lognormal prediction of $\frac{4}{9}$. It is tempting to try to place our numerical data (table 4) on this graph. Run 3*b* did not give a reliable first-derivative flatness because of insufficient resolution at low wavenumbers, but we would estimate it to be $\sim 4{\cdot}5$ at R_λ of 50. Plotted against what we believe to be a correct second-derivative flatness of 9·3 gives a point below and to the right of experiment. Clearly our $F_{u'}$ is nearly a factor of 2 too large at these Reynolds numbers. We do not understand the source of the discrepancy although, as we argued in subsection 1 of § 3(*c*), the numerical value of $F_{u'}$ seems firm.

Apart from using wires convincingly small enough to resolve the first- and second-derivative flatness, it would be of great interest to measure quantities such as $\langle(\partial u_2/\partial x_1)^4\rangle$ and $\langle(\partial u_1/\partial x_1)^2(\partial u_2/\partial x_1)^2\rangle$. All attempts to parametrize intermittency to date simply count the factors of the local dissipation rate that enter a given average. There is no freedom in the phenomenological description to treat tensor elements with

the same dimensions but that are not related by homogeneity or isotropy (e.g. $\langle\omega^4\rangle$ *vs.* $\langle(\mathrm{tr}\,(e^2))^2\rangle$) differently (Siggia 1981).

Lastly, the reader should be reminded that it has not proven feasible to implement numerically the iterative method proposed in the introduction for mapping out a large range of scales. Posing the problem has at least led us to structure our simulations rather differently than is conventional and to insist on a comparison between the 32^3 and 64^3 codes. The technique outlined in § 1 bears some resemblance to Wilson's renormalization group (Wilson & Kogut 1974).

The author is indebted to Dr G. S. Patterson, for making his spectral code available, together with T. Bell and J. Curry for assistance in modifying it for the Cray-1. K. G. Wilson contributed many useful ideas on how to implement a renormalization group numerically. Our computations were carried out at the National Center for Atmospheric Research, sponsored by the National Science Foundation.

REFERENCES

BATCHELOR, G. K. & TOWNSEND, A. A. 1949 *Proc. Roy. Soc.* A **199**, 238.

BETCHOV, R. 1956 *J. Fluid Mech.* **1**, 497.

CHAMPAGNE, F. 1978 *J. Fluid Mech.* **86**, 67.

CLARK, R. A., FERZIGER, J. H. & REYNOLDS, W. S. 1979 *J. Fluid Mech.* **91**, 1.

FRISCH, U., SULEM, P. L. & NELKIN, M. 1978 *J. Fluid Mech.* **87**, 719.

KOLMOGOROV, A. N. 1941 *C. r. Acad. Sci. U.S.S.R.* **30**, 301, 538.

KRAICHNAN, R. H. 1974 *J. Fluid Mech.* **62**, 305.

KRAICHNAN, R. H. 1976 *J. Atmos. Sci.* **33**, 1521.

KUO, A. Y.-S. & CORRSIN, S. 1971 *J. Fluid Mech.* **50**, 285.

KUO, A. Y.-S. & CORRSIN, S. 1972 *J. Fluid Mech.* **56**, 447.

MANDELBROT, B. 1976 In *Proceedings Journées Mathématiques sur la Turbulence* (ed. R. Teman). Springer.

MONIN, A. S. & YAGLOM, A. M. 1975 *Statistical Fluid Dynamics*, vol. 2. Massachusetts Institute of Technology Press.

ORSZAG, S. A. & PATTERSON, G. S. 1972 In *Statistical Models and Turbulence* (ed. M. Rosenblatt & C. Van Atta), p. 127. Springer.

PATTERSON, G. S. & ORSZAG, S. A. 1971 *Phys. Fluids* **14**, 2538.

SAFFMAN, P. G. 1968 In *Topics in Nonlinear Physics* (ed. N. Zabusky), p. 485. Springer.

SIGGIA, E. D. 1977 *Phys. Rev.* A **15**, 1730.

SIGGIA, E. D. 1978 *Phys. Rev.* A **17**, 1166.

SIGGIA, E. D. 1981 *Phys. Fluids.* (Submitted.)

SIGGIA, E. D. & PATTERSON, G. S. 1978 *J. Fluid Mech.* **86**, 567.

VAN ATTA, C. W. & ANTONIA, R. A. 1980 *Phys. Fluids* **23**, 252.

WILSON, K. G. & KOGUT, J. 1974 *Phys. Rev.* C **12**, 76.

WYNGARD, J. C. 1968 *J. Sci. Inst.* **1**, 1105.

WYNGAARD, J. C. 1969 *J. Sci. Inst.* **2**, 983.

WYNGAARD, J. C. 1971 *J. Phys. Fluids* **14**, 2052.